Janus-faced graphene substrate stabilizes lithium metal anode

Jingjing Ma [a], Jinlong Yang [c,*], Yuwei Zhao [a], Qianli Ma [a], Zhe Wang [b], Wei Qian [b], Bin Xia [b], Lun Li [b], Weihao Zeng [a], Junxin Chen [a], Hanwen Xu [a], Shuaishuai Chen [a], Daping He [b,*], Zhenbo Wang [c], Shichun Mu [a,*]

[a] State Key Laboratory of Advanced Technology for Materials Synthesis and Processing, Wuhan University of Technology, Wuhan 430070, Hubei, China
[b] Hubei Engineering Research Center of RF-Microwave Technology and Application, Wuhan University of Technology, Wuhan 430070, Hubei, China
[c] Guangdong Research Center for Interfacial Engineering of Functional Materials, College of Materials Science and Engineering, Shenzhen University, Shenzhen 518060, China

ARTICLE INFO

ABSTRACT

The dendrite growth and irreversibility of lithium (Li) metal anode seriously hinders the wide-scale application of high-energy–density rechargeable batteries. Here, we report a thin Janus-faced graphene substrate, consisting of lithiophilic-lithiophobic faces separately, for Li plating/stripping. The visualized analysis demonstrates that the unique Janus-faced graphene structure provides different lithiophilic sites and pore channels to steer the Li electrodeposition and suppress the dendrite growth. As expected, the Janus-faced graphene anode achieves long-term Li plating/stripping with high Coulombic efficiency, small polarization and stable cycling throughout the symmetry, asymmetry and LiFePO$_4$ full cells. Such an encouraging strategy for reversible Li plating/stripping provides a promising way to design long-life carbon-base anode materials for Li metal batteries.

1. Introduction

With the development of society, a steady increase in the demand for high energy density lithium (Li) ion batteries (LIBs) has rekindled interests in Li metal anode, which features high theoretical specific capacity (3860 mAh g^{-1}) and low electrode potential (-3.04 V $vs.$ SHE). [1–4] However, due to the extremely high chemical activity, Li metal will react with the electrolyte to increase the consumption of Li and electrolyte, which induces rupture and regeneration of solid-electrolyte interphase (SEI), increasing the voltage polarization. Additionally, the uneven plating and dendrite growth of Li will lead to a series of problems, including the infinite volume expansion, formation of dead Li and short circuit. These problems will inevitably result in low Coulombic efficiency (CE), short cycling-life, and even thermal runaway that may cause the safety accident.[5] Therefore, Li metal anodes still face many challenges, and the corresponding strategy needs to be explored for practical applications.

Currently, considerable efforts have been devoted to tackling the severe problems of Li metal anodes, such as developing a stable interfacial layer to improve the chemical and mechanical stability to inhibit Li dendrites,[6–12] adding functional additives (such as LiNO$_3$, LiF, $etc.$) in electrolytes to form stabilized SEI,[13–15] or employing Li binary alloy protective layers [16] and high-modulus solid electrolytes to prevent the dendrite growth.[17–21] Although these strategies can mitigate the deterioration of Li metal anodes to a certain extent, the liquid electrolyte additives is gradually depleted, affecting the properties of SEI during the battery cycle,[2,22–24] and the current solid electrolytes have poor ionic conductivity and large interfacial resistance.[25–27] In addition, the surface modification cannot effectively accommodate the infinite volume changes of Li metal. In particular, the development of 3D-structured conductive scaffold arouses great attentions, such as 3D porous metal framework,[28–32] 3D carbon composite matrix,[33–36] and 3D ion-conducting matrix.[37] The 3D-structured metal framework is not only a host material for providing high specific areas to accommodate Li, but also enable the homogenization of Li-ion flux to inhibit the growth of Li dendrites.[38–40] Alp Yurum $et\ al.$ [41] also prepared reduced graphene oxide (rGO) with N-doping after annealing rGO in NH$_3$ atomsphere.[42] As the content of pyridinic N increased, the Li storage capacity was enhanced. However, the SEI stabilization in a 3D high-surface-area of Li composite anode over long periods of time is doubtable. This is because when the interior space is filled with Li deposition, dendrites still tend to spill out.[43] In addition, the practical applications are limited by complicated and time-consuming building process of the large-scale elaborate specific structure.[44]

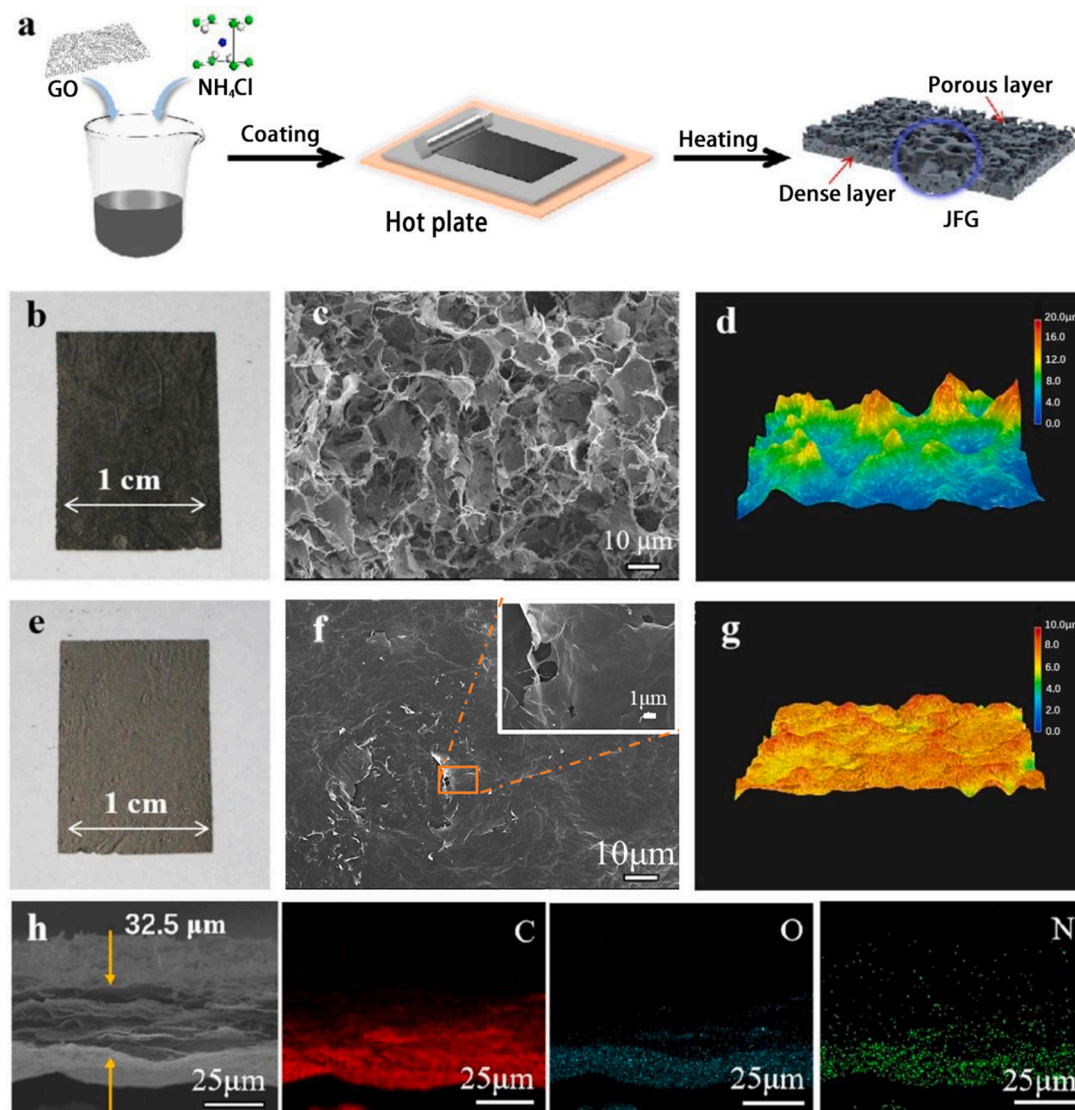**Fig. 1.** Schematic illustration of the fabricated JFG and morphology features. (a) Synthesis route, the final product has porous (macropores) and N-poor layer, dense (nanopores) and N-enriched layer, (b, e) optical images, (c, f) SEM images and (d, g) super-large depth of field 3D microscopic images of the (b-d) porous and (e-f) dense layers. (h) Cross-section SEM image and the corresponding C, O, N elemental mapping for JFG.

Herein, we design a 3D lithiophilic-lithiophobic Janus-faced graphene (JFG) substrate for long-life and dendrite-free Li metal batteries, which has a dense surface and a macroporous surface for Li deposition. Such a 3D JFG structure is created due to the different content distribution of ammonium chloride, as a gas foaming agent, during the heat treatment. By electrodepositing Li metal in the well-defined 3D JFG structure, the obtained composite anode exhibits long-term Li plating/stripping with high CE, small polarization and stable cyclability in the symmetry, asymmetry and LiFePO$_4$ full cells. It can be found that the macropore-enriched graphene away from the cathode provides space for Li storage. What's more, the graphene near the cathode has relatively dense structure with nanopore channels which allow Li ions to penetrate but inhibit the Li dendrite growth. Meanwhile, because of rich nitrogen-doping, the dense layer of graphene can supply the lithiophilic sites that permit Li to be uniformly deposited into the inner pore structure. These features demonstrate that the self-supporting JFG structure with a lithiophilic dense surface and a lithiophobic porous side can facilitate the development of safe and stable Li metal anodes.

2. Experimental section

2.1. Preparation of JFG anodes

In a typical synthesis, 1 g graphene oxide (GO, purchased from Wuxi Chengyi Education Technology Co., Ltd.) was dispersed into 30 ml deionized water to form a GO suspension, and 0.5 g NH$_4$Cl (Alfa Aesar, AR) was dissolved in 10 ml deionized water. After mixture with mechanical stirring, the formed slurry was scraped smoothly onto the surface of polyethylene terephthalate (PET) films, with the controlled thickness of 4 mm. After drying at 60 °C, the fabricated films were peeled off and put in an annealing furnace for 2 h heating under Ar atmosphere from room temperature to 1000 °C at a rate of 5 °C min^{-1}. Finally, the product with two-sided properties was obtained and named as JFG.

3. Results and discussion

3.1. Synthesis and characterization

The synthesis route for JFG is shown in Fig. 1a. First, graphene oxide
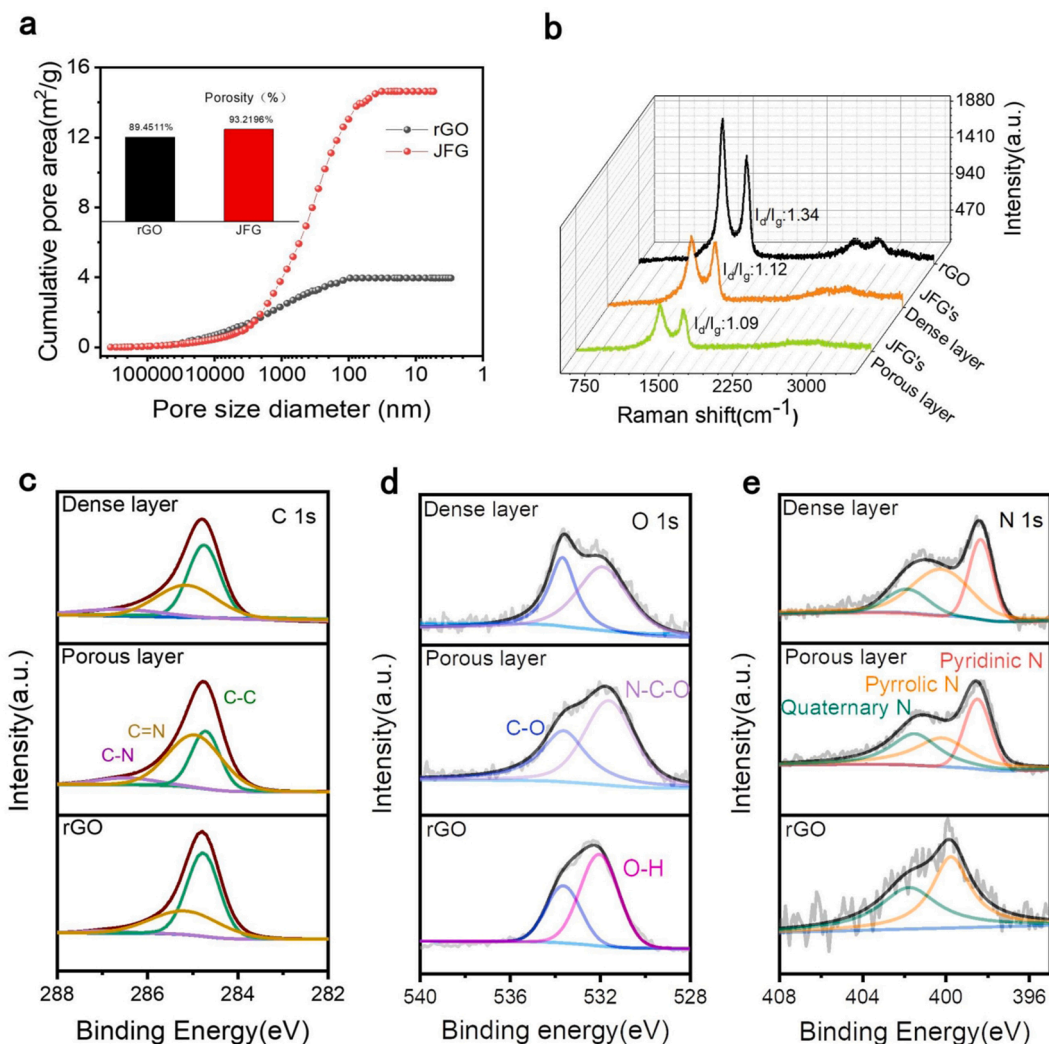
Fig. 2. (a) Pore diameter, porosity of mercury porosimetry measurement, and (b) Raman spectra for rGO and JFG, (c-e) binding energies of (c) C 1s, (d) O 1s and (e) N 1s in rGO and JFG.

(GO) as a starting material, and NH_4Cl gas foaming agents were mechanically mixed in deionized water to obtain a slurry with a certain viscosity. Then the composite film with a large area was prepared *via* uniformly coating the slurry on a hot plate and then drying. When peeled off, it can be found that both sides of the film show a difference in color (Figure S1), due to the tunable density of NH_4Cl by regulating the heating plate. Few NH_4Cl crystals formed on GO sheets near the heater, while high concentration of NH_4Cl crystals scattered on the upper graphene sheets. X-ray diffraction (XRD) patterns (**Figure S2**a) further validated the composition of both sides of GO composite film. Last, the GO composite film was calcined at 1000 °C for 2 h to remove oxygen-containing functional group and realize the N-doping, thus obtaining a graphene substrate with two different sides with different pore sizes and doping contents. On one side, it featured a porous (macropores) structure and N-poor doping, and on the other side it was dense (nanopores) and N-enriched, leading to the formation of the so called JFG structure (**Figure S2**b).

The optical images of both sides of JFG film in Fig. 1b and 1e show a distinct dark gray and light gray. Furthermore, the morphology features of both sides of JFG film were investigated by scanning electron microscope (SEM) (Fig. 1c and 1f) and super-large depth of field 3D microscopy (Fig. 1d and 1g). The one side of GO film is occupied by large pores with a depth of ~ 10 µm, while the other side possesses a relatively dense structure with small pores and average depth ~ 20 µm. By means

of energy dispersive spectrometer (EDS) mapping, higher O and N content can be observed near the dense graphene, but it is relatively rare at the porous layer. Thus, we can conclude that the main reasons for the color difference come from two factors: different apertures and gradient N-doping.

The key to establishing JFG is gas foaming agents. NH_4Cl is not only the N source, but also foamed to build a 3D porous network,[45] since NH_4Cl can be decomposed into NH_3 and HCl during the high-temperature carbonization process. The resulting NH_3 can be further combined with the carboxyl group of GO by means of a dehydration-condensation reaction, and then the *in-situ* introduction of N atoms into the carbonized graphite lattice. The release of a large amount of NH_3 and the instantaneous high pressure generated internally can endue the carbon substrate with a fluffy porous structure.

Besides the SEM observation, Mercury porosimetry was used to identify the pore distribution of JFG and pure graphene film. According to the pore size distribution of rGO and JFG shown in Fig. 2a, the total pore volume augments with blend of NH_4Cl. A large number of wrinkles and pores endow the JFG composite with a large pore area of 14.64 m^2 g^{-1} and a high pore volume of 8.20 cm^3 g^{-1}, which can adapt to large volume changes in the process of Li plating/stripping and reduce local current density. Especially, from the pore size-area curves at the beginning, the small pore area indicates that the proportion of macropores over 10 µm is very small in both rGO and JFG. However, the pore
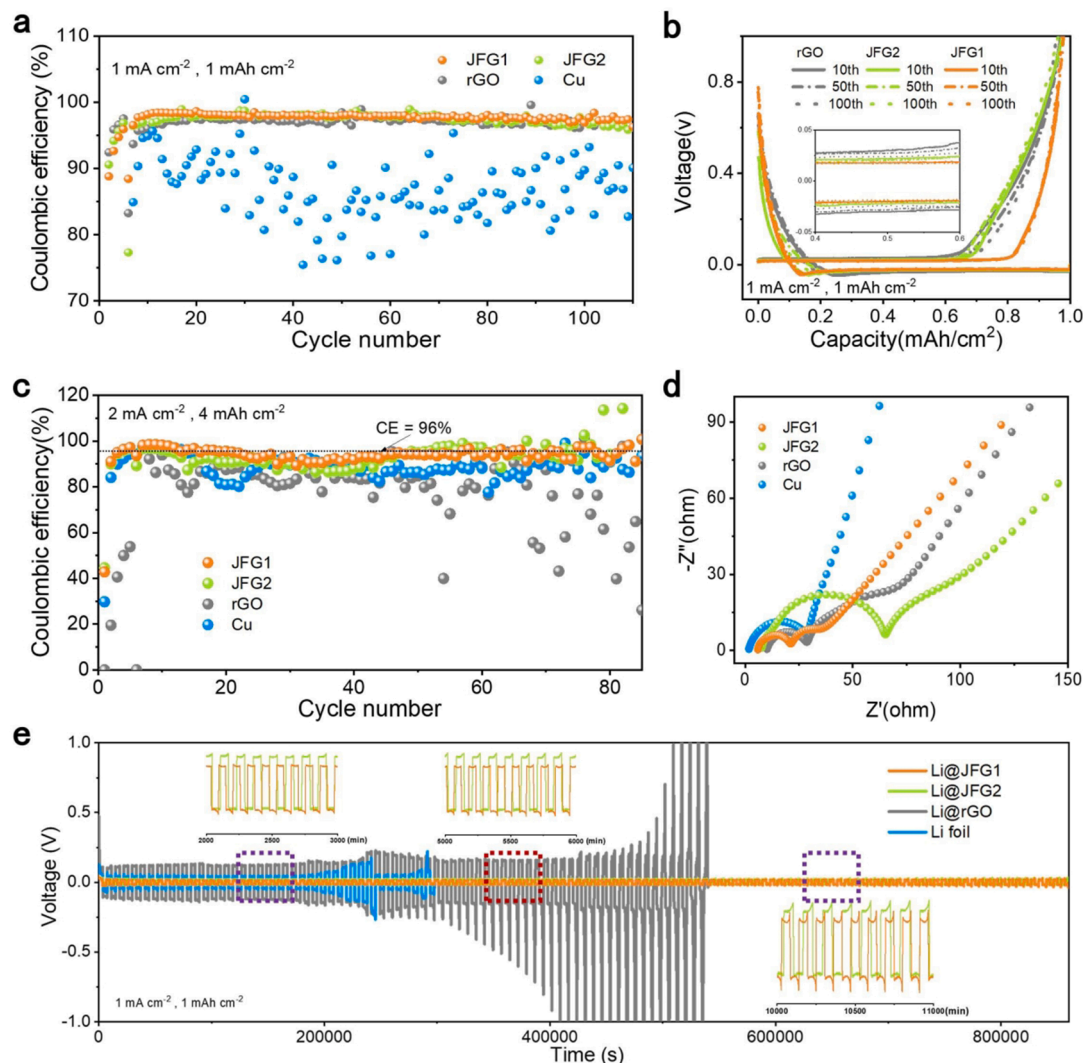
Fig. 3. Electrochemical performance of Li deposition/stripping on JFG1, JFG2, rGO and Cu electrode. (a) Li cycling CE, (b) Voltage-capacity curves of lithium electrodeposition/stripping on different electrodes at a current density of 1 mA cm^{-2} and a capacity of 1 mAh cm^{-2}. (c) Li cycling CE at a current density of 2 mA cm^{-2} and a capacity of 4 mAh cm^{-2}. (d) Impedance spectroscopy of lithium electrodeposition/ stripping on different electrodes after 50 cycles. (e) Voltage profiles of Li plating/stripping in different symmetric cells with current density of 1 mA cm^{-2} for 1 mAh cm^{-2}.

area of JFG from 0.1 μm to 20 μm significantly increases to 14 m^2 g^{-1}, which is three times larger than that of rGO (4 m^2 g^{-1}). Therefore, the addition of NH$_4$Cl can significantly improve the specific surface area of graphene, thus enhancing the penetration ability of Li-ions and electrolyte (Figure S3).

In addition, the graphitization and chemical structure of the two carbon materials were characterized by Raman spectroscopy (Fig. 2b). Compared with rGO, the I$_D$/I$_G$ values (~ 1.1) for both sides of JFG is smaller than that (1.34) of rGO, indicating the increased degree of graphitization and crystallinity for JFG. The increase in the intensity of the second-order scattering around the graphene-related 2D band (about 2700 cm^{-1}) [46] further proves the successful reduction of GO to rGO, which shows that the porous surface was reduced more completely than the relatively dense layer, and also indicates the turbine stratigraphic arrangement of the graphene layer. These results confirm the synergistic effect of thermal and NH$_3$ reduction for the formation of the 3D JFG structure.

To further explore the different effects of pore size and N-doping content surfaces on Li deposition, we employed molten Li to monitory the Li-friendly properties of both sides of JFG (Figure S4). It can be found that the porous layer is too lithiophobic, and the opposite effect of the dense layer to Li. According to the EDS mapping, the N elements are

gradient doping. It is well known that graphene has poor wettability to Li, which is likely to cause uneven deposition of Li.[47] This is why some researchers have carried out lithiophilic modification on the carbon matrix (such as lithiophilic functional group,[20] insertion of nucleation seed[48]). Meanwhile, it has also been reported that N-doped graphene, with pyridinic or pyrrolic nitrogen that belongs to lithiophilic functional groups, can provide more lithium nucleation sites and smaller nucleation overpotentials to the copper foil.[20]

X-ray photoelectron spectroscopy (XPS) was further used to explore the formation of lithiophilic-lithiophobic layers. As shown in Figure S5, pure rGO is N-free (Fig. 2c and 2e). However, the C 1s binding energies of JFG samples (Fig. 2c) show the main peak at around 284.8 eV, corresponding to sp2 carbon, and the peaks at 285.8 and 287.6 eV, are assigned to C = N bonds and C-N species, respectively.[49] Meanwhile, N-C-O and C-O groups can be observed in the XPS of O 1s (Fig. 2d). Furthermore, three N-species including pyridine nitrogen (pnN, 398.5 eV), pyrrole nitrogen (prN, 400.2 eV) and quaternary nitrogen (qN, 401.5 eV) (Fig. 2e) as lithiophilic functional groups are distributed in graphene skeleton of JFG. Combined with EDS mapping (Fig. 1h), it indicates that the N element gradient doping is one of the main reasons for the formation of the lithio-philic/phobic gradient layer.

In addition to the lithiophilic functional group, the JFG provides a 3D
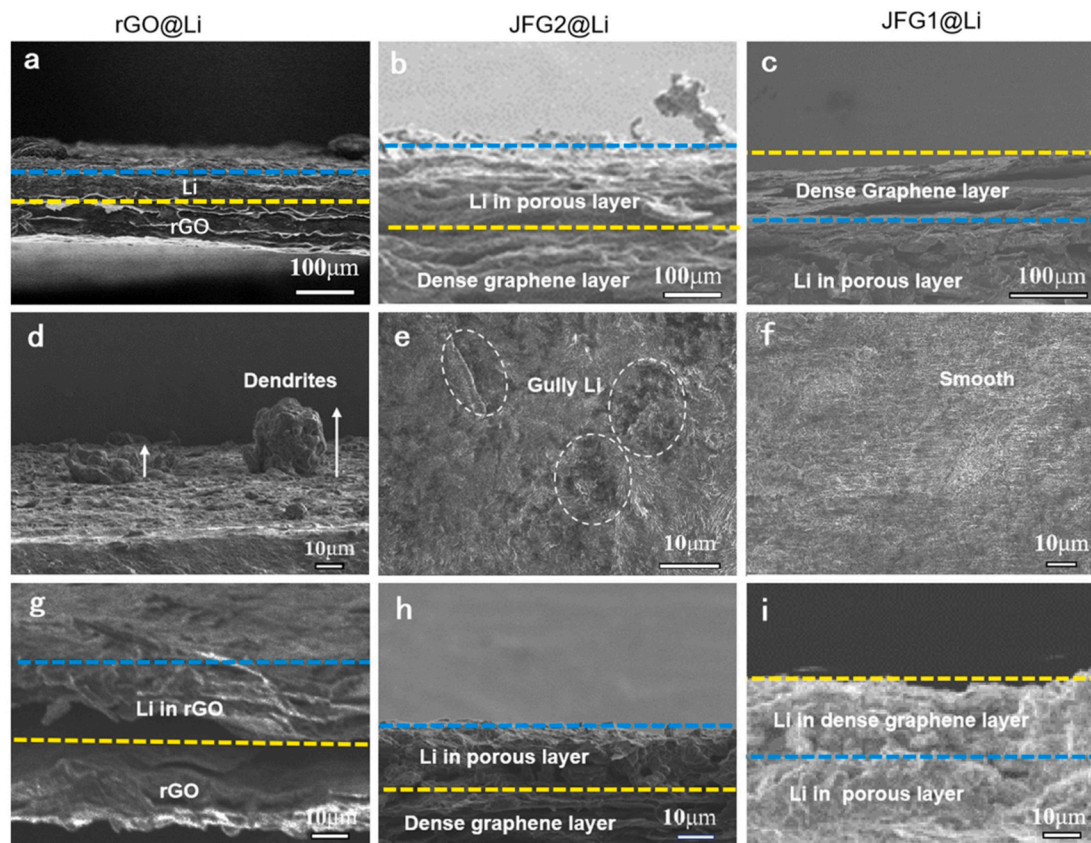
Fig. 4. Deposition and cycling behaviors of lithium on different electrodes. Cross-sectional and top-view SEM images of (a, d) rGO, (b, e) JFG2, and (c, f) JFG1. (a-c) Cross-sectional SEM images of three sample electrodes after the first Li-deposition. (d-f) Top-view SEM images of three sample electrodes after the first Li-stripping step. (g-i) Cross-sectional SEM images of (g) rGO, (h) JFG2 and (i) JFG1 after 50 cycles. The cycling current density and capacity were 1 mA cm^{-2} and 1 mAh cm^{-2}, respectively.

capillary effect, which also plays a vital role in capillary action to induce Li inner deposition. The Equation (1) as follow express capillary force [50]:

$$P_{cap} = \frac{2\sigma}{r_{eff}} \tag{1}$$

where σ is the surface tension of liquid and r_{eff} is the effective capillary radius. Obviously, r_{eff} is inversely proportional to P_{cap}. This also can be explained by the imperfect regions of micropore layers due to strong chemical reaction, which compromises the capillary effect by the equation.

3.2. Electrochemistry of Li-plating/stripping.

To investigate the effect of JFG on the electrochemical properties of Li-plating/stripping, we used two different faces of JFG as the Li-deposition interface: JFG1 is the lithiophilic dense layer acting as induced Li deposition interface, while JFG2 is the porous layer as a spacer. Also, rGO and Cu foil were applied as control sample electrodes. The effect of different substrates on electrochemical performance of Li plating/stripping was firstly evaluated by CE cycling tests with the same ether electrolyte (Details seeing Experimental Parts). These electrodes were used to pair with Li foil. Fig. 3a shows the CEs of substrates at current density of 1 mA cm^{-2} and capacity of 1 mAh cm^{-2}. It can be seen that porous graphene substrates, including rGO, JFG1 and JFG2, have a significantly improved CE of > 95% for over 110 cycles compared with the controlled Cu electrodes. Especially, among them, JFG1 shows the highest CE of 98%, which demonstrated its improved reversibility of galvanostatic Li plating/stripping. Furthermore, even under deep Li

plating/stripping (4 mAh cm^{-2}) at a high current density (2 mA cm^{-2}), JFG1 presents a CE of 96.1% and stable charge–discharge profiles within 80 cycles (Fig. 3c), which also outperforms the other two graphene-based substrates (rGO and JFG2). These results prove that JFG1 with dense lithiophilic interface enables homogeneous Li transmission and improves the cycle stability of the Li-metal anode. Such a greatly improved CE benefits the future high energy density battery system which requires high reversibility of Li electro-plating/stripping at high current densities and high areal capacity cycling states.

Meanwhile, the Li plating/stripping kinetics in different substrates was also investigated. By observing from the voltage-capacity curves (Fig. 3b), it reveals that the charge platform capacity of JFG1 is larger than that of the others. Meanwhile, for JFG1 the voltage drop in the nucleation stage is smoother, both the nucleation overpotential (Figure S6) and polarization voltage (inset of Fig. 3b) are also smaller than other electrodes. The fast kinetics could be attributed to the presence of lithiophilic N, O-containing functional groups and the special pore structure in the interface near the Li plate, which is helpful to regulate the SEI structure and facilitate the smooth stripping and delivery of Li into the electrolyte. The lowest charge transfer impedance for JFG1 (Fig. 3d) further proves the fast Li plating/stripping kinetics. Therefore, the Janus-faced structure with lithiophilic interface is more conducive to improving the uniformity of Li deposition when the current density becomes large, while other controlled electrodes leads to serious loss of Li and promote the growth of more dendrites.

In addition, to reveal the property-increasing effect, the cycling stability of symmetric cells was also performed with Li foil, Li@rGO, Li@JFG2, and Li@JFG1 as Li electrodes, respectively. The stability test of constant current cycle was carried out to explore the influence of this
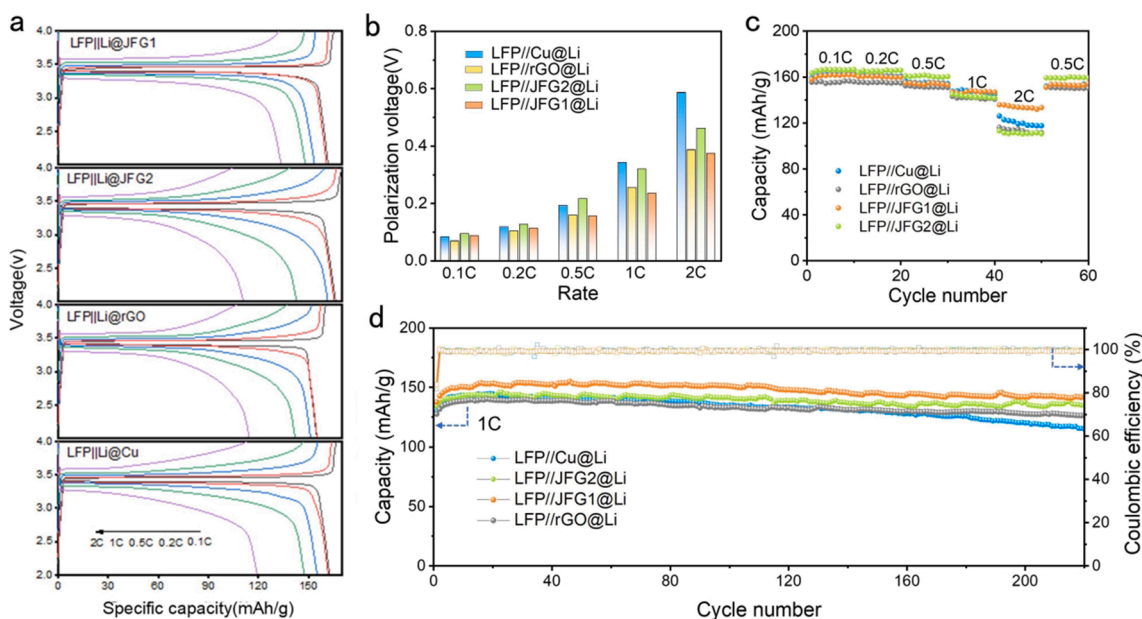
Fig. 5. Electrochemical performance of LiFePO$_4$ (LFP) full cells. (a) Typical charge/discharge curves, (b) polarization voltage and (c) rate capability at different current density from 0.1 to 2 C, (d) long-term cycling life at 1 C for the LFP//Li@rGO, LFP//Li@JFG1 and LFP//Li@JFG2 and LFP//Li@Cu cells.

skeleton structure on polarization. The cycling properties of Li foil, Li-rGO, Li-JFG2, and Li-JFG1 at 1 mA cm^{-2} with areal capacity of 1 mAh cm^{-2} are present in Fig. 3e. Obviously, the symmetric cell with Li-JFG1 displays the lowest and steady voltage polarization, with only ~ 15 mV over in whole process. In contrast, the exposed anode of Li metal exhibits a sharp voltage fluctuation in the initial few cycles, and then a micro-short circuit occurs followed by sharp raises and drops. The overpotential of JFG1 is slightly smaller than that of JFG2. These findings testify that Li is even smooth owing to the pore-forming method and abundant Li nucleation sites, restraining the formation of dendrites, and undoubtedly improving the long-term cycling stability of Li metal anode.

3.3. Deposition and cycling behaviors of Li@JFG1.

The Li electro-plating/stripping process on the electrode determines the cycle stability and capacity utilization. Cycling behaviors of different electrodes after Li deposition and were investigated by the cross-section and surface images (Fig. 4). From Fig. 4a, it can be seen that the solvated Li ions were more likely to be shed the solvent molecules and electrochemically reduced into adatoms, then deposited on the surface of rGO electrodes. Fig. 4b shows that Li was deposited in the porous layer of JFG2 electrodes. The surface structures of composite Li@rGO anodes in Fig. 4d exhibit some obvious Li dendrites, which could be caused by locally increased current densities on the upper surface of electrode when the Li ion-transport path was further blocked and only deposited on the surface of previously deposited Li metal. For JFG1 electrode, Li ions can be induced by lithiophilic interfaces and then pass through the nanopores to deposit inside of the macroporous layer (Fig. 4c). This feature results in homogeneous Li deposition on the outer surface of matrix and layered structure is well maintained (Fig. 4f). By contrast, we found that during the subsequent cycle, rGO electrode shows large dendritic residues (Fig. 4d), while different forms of "dead Li" and SEI remain on the JFG2 surface which is highly rough and riddled, as confirmed by the vertical view SEM image (Fig. 4e). In contrast, Li@JFG1 electrode reveals a flat surface without dendrites, and maintains a good layered structure (Fig. 4f). Especially, after 50 cycles, for Li@rGO and Li@JFG2, the Li was preferentially deposited on the surface with uneven distribution, exhibiting a greater amount of dead Li, with a

high degree of roughness (Fig. 4g and 4h). In comparison, even after 50 cycles, Li was still evenly filled in the porous layers of JFG1, indicating its good structure retention (Fig. 4i). Notably, the depositing morphologies of the JFG electrodes at 4 mAh/cm^2 and after 250 cycles further prove the advantages of JFG1 scaffold suppressing the Li dendrite growth in high capacity and prolonging cycle life situation (Figure S7). Therefore, the lithiophilic dense interface near the cathode and the lithiophobic pore-enriched surface away from the cathode are beneficial to the reversible Li deposition/stripping.

3.4. Electrochemical performance of full cells.

To investigate the electrochemical performance of Li@Cu, Li@rGO, Li@JFG1, Li@JFG2, four types of full cells paired with LFP cathode were evaluated and compared in detail. Fig. 5a shows the charge/discharge curves of full cells at different current densities from 0.1 C to 2 C (the capacity ratio of N/P is ~ 4.1). The four cells show much difference in capacity and voltage platform. The main reason for this phenomenon is due to the difference in composite Li anodes, in which all their reversibility, stability and kinetics affect the electrochemical performance of full cells. First, we compared the polarization voltage (ΔV) calculated from voltage difference between charging/discharging platforms when the battery reached half of LFP theoretical capacity (85 mAh/g). As shown in Fig. 5b, among LFP//Li@rGO, LFP//Li@JFG1 and LFP//Li@JFG2 and LFP//Li@Cu cells, the ΔV value of the LFP//Li@JFG1 cell is the smallest at all current densities. Especially, the ΔV of the LFP//Li@JFG1 cell is 0.38 V at the high current density of 2 C, less than half one of the LFP//Li@Cu cell (0.58 V), demonstrating fast Li transport kinetics from the LFP cathode to the Li@JFG1 composite anode. Then, the rate capability of LFP//Li@JFG1 was also investigated. As shown in Fig. 5c, the LFP//JFG1@Li cell can keep capacity retention of 84% from 0.1 C to 2.0 C, higher than that of other cells including LFP//Li@rGO (71.6%) and LFP//Li@Cu (74.2%). Furthermore, as the current density decreases, the capacity is also recovered by degrees, implying the JFG1 structure is the optimal solution to tackle various unstable issues of Li anode and improve the battery life.

For practical applications, it is significant for a battery to achieve high capacity with long cycling life, even at high current densities. Fig. 5d displays the cycling performance of four full cells at a current
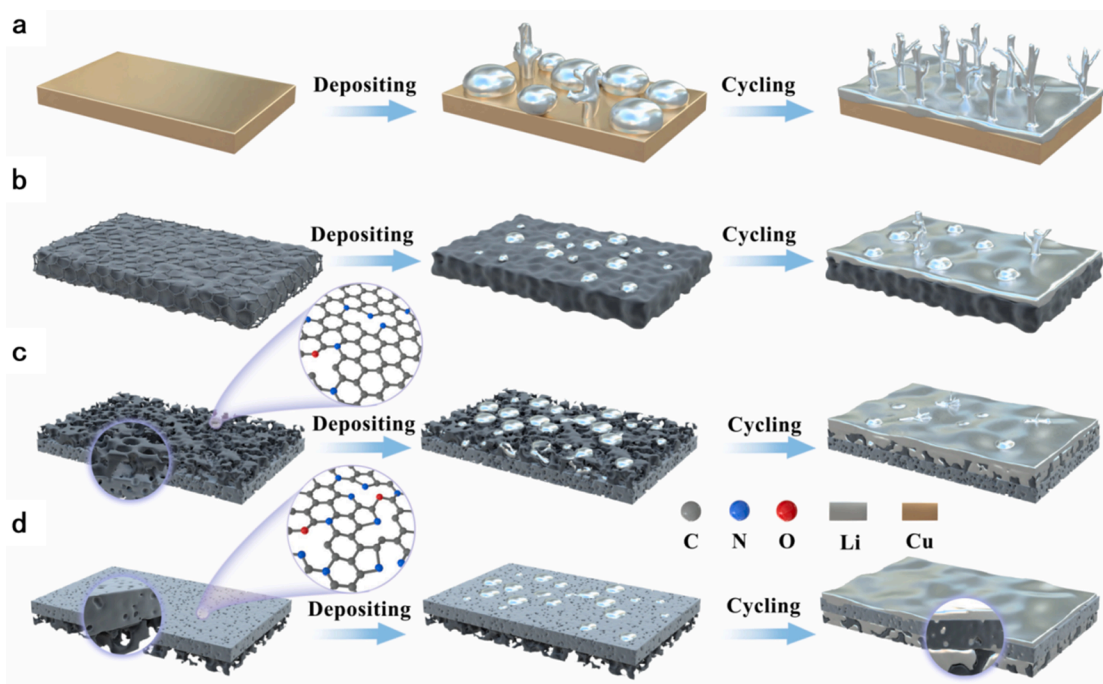
Fig. 6. Schematic of lithium plating/stripping process on (a) Cu, (b) rGO, (c) JFG2 and (d) JFG1 electrodes.

density of 1 C. Notably, the discharge capacity of the LFP//Li@JFG1 cell is higher than that of the other three cells, and the battery retains a capacity of over 143 mAh/g up to 220 cycles, corresponding to a capacity retention of 94%. What's more, the corresponding CE maintains as high as 99.5%, illustrating the superior electrochemical reversibility and structure stability of electrodes. Importantly, to evaluate the stability of the LFP||Li@JFG1 full battery, high mass loading of 11.5 mg/cm^2 for LFP at cathodes were performed. As shown in Figure S8, the capacity of LFP||Li@JFG1 full battery at 1 C still maintains at 132 mAh/g after 40 cycles. These results clearly show that the Li@JFG1 anode has good compatibility with conventional electrolyte and LFP cathodes, which has a high potential to develop high-power and long-life batteries, meeting the needs of batteries in practical applications.

4. Mechanism of suppressing Li dendrites growth in Janus-faced graphene anode

Next, we further elucidate the mechanism of the JFG1 structure during charge and discharge process. Based on experimental results and literature reports, Li prefers to rigidly plating/stripping on the upper surface of Cu and 2D graphene electrodes after long-time infusing (Fig. 6a and 6b). The accumulated Li on the upper surface further obstructs ionic transport by physically cutting off the electrolyte from entering into the interior, thereby aggravating the upper overgrowth, and accelerating the SEI rupture and damage of the valid internal electrode surfaces. The increased vast leftover dead Li and SEI on the upper surface further downgrade the anode reversibility, block the incoming ion-transport path, and expedite the nonuniform of Li accumulation, resulting in the dendrite growth during repetitious Li plating/stripping cycles. Moreover, the severe deformation of the electrode induces amplified consumption of electrolyte and massive uncontrollable SEI formation.

The JFG structure, with lithiophilic dense surface and lithiophobic macropore-enriched surface, has many advantages (Fig. 6d), but which side is better for Li plating/stripping needs to be determined. First, for the macroporous surface pairing to Li metal, Li is mainly filled on the upper surface. Although the overgrown Li is reduced compared to the pure rGO film, the moss-like dendrites still gather on the surface

(Fig. 6c). In contrast, as presented in Fig. 6d, Li can be uniformly deposited into the matrix through the nanopores and reach the bottom where there is a large Li-storing space. The lithiophobicity of the lower surface can basically maintain the previous layered structure after stripping. Therefore, the JFG electrode exhibits a low nucleation overpotential and a highly reversible Li plating/stripping cycle.

5. Conclusions

In conclusion, large-area graphene "host" framework was optimized to obtain the JFG1 film composed of the lithiophilic dense surface and lithiophobic micropore-rich surface on the obverse side and the reverse side, which greatly improved the composite anode through two crucial effects. First, since the lithiophilic N-containing functional groups, JFG1 is capable of regulating the metallic Li nucleation process through electrodeposition. Second, the porous layer with high specific surface area is beneficial to storage of Li, and then dendrites can be inhibited by the dense layer after filling the inner space. As a result, the JFG1 electrode in LFP//Li@JFG1 full cells can achieve a stable cycling for ∼ 200 cycles at 1 C with limited Li source, which exhibits high cycling efficiency and superior rate capability. Undoubtedly, this finding will shed a new light on surface structure engineering for significantly boosting the performance of Li metal batteries as well as the large-scale application of high-energy Li batteries.

Declaration of Competing Interest

The authors declare that they have no known competing financial interests or personal relationships that could have appeared to influence the work reported in this paper.

Acknowledgments

Appendix A. Supplementary data

Supplementary data to this article can be found online at https://doi.org/10.1016/j.cej.2021.133561.

References

[1] M. Armand, J.M. Tarascon, Nature 451 (2008) 652–657.
[2] W. Xu, J.L. Wang, F. Ding, X.L. Chen, E. Nasybutin, Y.H. Zhang, J.G. Zhang, Energy Environ. Sci. 7 (2014) 513–537.
[3] Y.M. Sun, N.A. Liu, Y. Cui, Nat. Energy 1 (2016).
[4] D.C. Lin, Y.Y. Liu, Y. Cui, Nat. Nanotechnol. 12 (2017) 194–206.
[5] D. Aurbach, E. Zinigrad, H. Teller, P. Dan, J. Electrochem. Soc. 147 (2000) 1274–1279.
[6] Y.X. Ren, L. Zeng, H.R. Jiang, W.Q. Ruan, Q. Chen, T.S. Zhao, Nat. Commun. 10 (2019).
[7] Y.-T. Weng, H.-W. Liu, A. Pei, F. Shi, H. Wang, C.-Y. Lin, S.-S. Huang, L.-Y. Su, J.-P. Hsu, C.-C. Fang, Y. Cui, N.-L. Wu, Nat. Commun. 10 (2019).
[8] C.-C. Su, M. He, R. Amine, Z. Chen, R. Sahore, N.D. Rago, K. Amine, Energy Stor. Mat. 17 (2019) 284–292.
[9] Y. Sun, C. Zhao, K.R. Adair, Y. Zhao, L.V. Goncharova, J. Liang, C. Wang, J. Li, R. Li, M. Cai, T.-K. Sham, X. Sun, Energy Environ. Sci. 14 (2021) 4085–4094.
[10] G. Zheng, Y. Xiang, S. Chen, S. Ganapathy, T.W. Verhallen, M. Liu, G. Zhong, J. Zhu, X. Han, W. Wang, W. Zhao, M. Wagemaker, Y. Yang, Energy Stor. Mat. 29 (2020) 377–385.
[11] B. Liu, M. Du, B. Chen, Y. Zhong, J. Zhou, F. Ye, K. Liao, W. Zhou, C. Cao, R. Cai, Z. Shao, Chem. Eng. J. 427 (2022) 131001.
[12] Z. Ju, X. Tao, C. Jin, H. Yuan, T. Yang, O. Sheng, T. Liu, Y. Liu, Y. Wang, F. Ma, W. Zhang, J. Nai. Chem. Eng. J. 408 (2021).
[13] J.M. Zheng, M.H. Engelhard, D.H. Mei, S.H. Jiao, B.J. Polzin, J.G. Zhang, W. Xu, Nat. Energy 2 (2017).
[14] A. Mauger, C.M. Julien, A. Paolella, M. Armand, K. Zaghib, Mat. Sci. Eng. R 134 (2018) 1–21.
[15] J. Alvarado, M.A. Schroeder, T.P. Pollard, X. Wang, J.Z. Lee, M. Zhang, T. Wynn, M. Ding, O. Borodin, Y.S. Meng, K. Xu, Energy Environ. Sci. 12 (2019) 780–794.
[16] Y. Xu, S. Zhao, G. Zhou, W. Chen, F. Zhou, Z. Rong, Y. Wu, J. Li, J. Guo, Y. Zhang, Acs. Appl. Energy Mater. 3 (2020) 2278–2284.
[17] H. Duan, Y.X. Yin, Y. Shi, P.F. Wang, X.D. Zhang, C.P. Yang, J.L. Shi, R. Wen, Y. G. Guo, L.J. Wan, J. Am. Chem. Soc. 140 (2018) 82–85.
[18] G.H. Yang, J.D. Chen, P.T. Xiao, P.O. Agboola, I. Shakir, Y.X. Xu, J. Mater. Chem. A 6 (2018) 9899–9905.
[19] Q. Pang, X. Liang, A. Shyamsunder, L.F. Nazar, Joule 1 (2017) 871–886.
[20] R. Zhang, X.R. Chen, X. Chen, X.B. Cheng, X.Q. Zhang, C. Yan, Q. Zhang, Angew Chem. Int. Ed. Engl. 56 (2017) 7764–7768.
[21] X. Zeng, L. Dong, J. Fu, L. Chen, J. Zhou, P. Zong, G. Liu, L. Shi, Chem. Eng. J. 428 (2022), 131100.
[22] W.Y. Li, H.B. Yao, K. Yan, G.Y. Zheng, Z. Liang, Y.M. Chiang, Y. Cui, Nat. Commun. 6 (2015).
[23] F. Ding, W. Xu, G.L. Graff, J. Zhang, M.L. Sushko, X.L. Chen, Y.Y. Shao, M. H. Engelhard, Z.M. Nie, J. Xiao, X.J. Liu, P.V. Sushko, J. Liu, J.G. Zhang, J. Am. Chem. Soc. 135 (2013) 4450–4456.
[24] G.A. Umeda, E. Menke, M. Richard, K.L. Stamm, F. Wudl, B. Dunn, J. Mater. Chem. 21 (2011) 1593–1599.
[25] N. Kamaya, K. Homma, Y. Yamakawa, M. Hirayama, R. Kanno, M. Yonemura, T. Kamiyama, Y. Kato, S. Hama, K. Kawamoto, A. Mitsui, Nat. Mater. 10 (2011) 682–686.
[26] H. Wan, G. Peng, X. Yao, J. Yang, P. Cui, X. Xu, Energy Stor. Mat. 4 (2016) 59–65.
[27] R. Bouchet, S. Maria, R. Meziane, A. Aboulaich, L. Lienafa, J.P. Bonnet, T.N. T. Phan, D. Bertin, D. Gigmes, D. Devaux, R. Denoyel, M. Armand, Nat. Mater. 12 (2013) 452–457.
[28] C.P. Yang, Y.X. Yin, S.F. Zhang, N.W. Li, Y.G. Guo, Nat. Commun. 6 (2015).
[29] A. Paolella, H. Demers, P. Chevallier, C. Gagnon, G. Girard, N. Delaporte, W. Zhu, A. Vijh, A. Guerfi, K. Zaghib, J. Power Sources 427 (2019) 201–206.
[30] M. Wan, S. Kang, L. Wang, H.-W. Lee, G.W. Zheng, Y. Cui, Y. Sun, Nat. Commun. 11 (2020).
[31] X. Ke, Y. Liang, L. Ou, H. Liu, Y. Chen, W. Wu, Y. Cheng, Z. Guo, Y. Lai, P. Liu, Z. Shi, Energy Stor. Mat. 23 (2019) 547–555.
[32] Q. Ran, L. Wang, L. Li, Y. Zhao, Z. Lu, S. Chen, J. Zou, P. Chen, J. Gao, X. Niu, Chem. Eng. J. 426 (2021), 130780.
[33] F.F. Liu, Z.W. Zhang, S.F. Ye, Y. Yao, Y.Y. Acta, Phys.-Chim. Sin. 37 (2021).
[34] C. Niu, H. Pan, W. Xu, J. Xiao, J.-G. Zhang, L. Luo, C. Wang, D. Mei, J. Meng, X. Wang, Z. Liu, L. Mai, J. Liu, Nat. Nanotechnol. 14 (2019) 594–+.
[35] L. Liu, Y.X. Yin, J.Y. Li, N.W. Li, X.X. Zeng, H. Ye, Y.G. Guo, L.J. Wan, Joule 1 (2017) 563–575.
[36] Y. Chen, X. Ke, Y. Cheng, M. Fan, W. Wu, X. Huang, Y. Liang, Y. Zhong, Z. Ao, Y. Lai, G. Wang, Z. Shi, Energy Stor. Mat. 26 (2020) 56–64.
[37] Z. Liang, K. Yan, G. Zhou, A. Pei, J. Zhao, Y. Sun, J. Xie, Y. Li, F. Shi, Y. Liu, D. Lin, K. Liu, H. Wang, H. Wang, Y. Lu, Y. Cui, Sci. Adv. 5 (2019).
[38] Q. Li, S.P. Zhu, Y.Y. Lu, Adv. Funct. Mater. 27 (2017).
[39] Z. Ju, J. Nai, Y. Wang, T. Liu, J. Zheng, H. Yuan, O. Sheng, C. Jin, W. Zhang, Z. Jin, H. Tian, Y. Liu, X. Tao, Nat. Commun. 11 (2020).
[40] R. Zhang, X. Shen, X.-B. Cheng, Q. Zhang, Energy Stor. Mat. 23 (2019) 556–565.
[41] A. Tasdemir, B.B. Kopuklu, A.C. Kirlioglu, S.A. Gursel, A. Yurum, Int. J. Hydrogen Energy 46 (2021) (1877) 11865–11877.
[42] J. Wang, H. Wang, J. Xie, A. Yang, A. Pei, C.-L. Wu, F. Shi, Y. Liu, D. Lin, Y. Gong, Y. Cui, Energy Stor. Mat. 14 (2018) 345–350.
[43] L.Y. Wang, X.Y. Zhu, Y.P. Guan, J.L. Zhang, F. Ai, W.F. Zhang, Y. Xiang, S. Vijayan, G.D. Li, Y.Q. Huang, G.P. Cao, Y.S. Yang, H. Zhang, Energy Stor. Mat. 11 (2018) 191–196.
[44] G.-L. Tian, M.-Q. Zhao, D. Yu, X.-Y. Kong, J.-Q. Huang, Q. Zhang, F. Wei, Small 10 (2014) 2251–2259.
[45] H. Jiang, J. Gu, X. Zheng, M. Liu, X. Qiu, L. Wang, W. Li, Z. Chen, X. Ji, J. Li, Energy Environ. Sci. 12 (2019) 322–333.
[46] A.C. Ferrari, J.C. Meyer, V. Scardaci, C. Casiraghi, M. Lazzeri, F. Mauri, S. Piscanec, D. Jiang, K.S. Novoselov, S. Roth, A.K. Geim, Phys. Rev. Lett. 97 (2006).
[47] J. Duan, Y. Zheng, W. Luo, W. Wu, T. Wang, Y. Xie, S. Li, J. Li, Y. Huang, Natl. Sci. Rev. 7 (2020) 1208–1217.
[48] H.S. Wang, X. Cao, H.K. Gu, Y.Y. Liu, Y.B. Li, Z.W. Zhang, W. Huang, H.X. Wang, J. Y. Wang, W. Xu, J.G. Zhang, Y. Cui, Acs. Nano. 14 (2020) 4601–4608.
[49] R. Wang, J. Yang, X. Chen, Y. Zhao, W. Zhao, G. Qian, S. Li, Y. Xiao, H. Chen, Y. Ye, G. Zhou, F. Pan, Adv. Energy Mater. 10 (2020).
[50] Y. Tang, D.X. Deng, L.S. Lu, M.Q. Pan, Q.H. Wang, Exp. Therm. Fluid Sci. 34 (2010) 190–196.